ASME Journal of Engineering for Gas Turbines and Power
Online journal at:
https://asmedigitalcollection.asme.org/gasturbinespower

A Dynamic Thickening Strategy for High-Fidelity Computational Fluid Dynamics Analyses of Multi-Regime Combustion

A. Ballotti[1]
Heat Transfer and Combustion Group,
DIEF Department of Industrial Engineering,
University of Florence,
Via S. Marta 3,
Florence 50139, Italy
e-mail: andrea.ballotti@unifi.it

S. Castellani
Heat Transfer and Combustion Group,
DIEF Department of Industrial Engineering,
University of Florence,
Via S. Marta 3,
Florence 50139, Italy
e-mail: simone.castellani@unifi.it

A. Andreini
Heat Transfer and Combustion Group,
DIEF Department of Industrial Engineering,
University of Florence,
Via S. Marta 3,
Florence 50139, Italy
e-mail: antonio.andreini@unifi.it

In this study, a dynamic thickening strategy for dynamic thickened flame model for large eddy simulations (DTFLES) application to multi-regime combustion is proposed. The main idea lies in using the numerical solution of an ordinary differential equation (ODE) as a thickening factor. The equation relates the time derivative of the local thickening factor to its production and destruction rates, which are proportional to the gap between the instantaneous value and optimal target values. The smoothness of the thickening factor in time is ensured by the ODE solution, while in space it is achieved through a mathematical function defined in a continuous flame index space. The equation is numerically integrated with a semi-implicit scheme by making use of the backward Euler formula. The strategy has been implemented in a commercial computational fluid dynamics (CFD) solver and it has been tested by performing Large Eddy Simulations of the hydrogen/air flame produced by the HYLON injector, which has been individuated as an interesting test case for the proposed dynamic strategy. Turbulence-chemistry interactions are recovered by means of a well-assessed subgrid efficiency model. Numerical results are compared with the experimental ones obtained at Institut de Mécanique des Fluides de Toulouse (IMFT).
[DOI: 10.1115/1.4066212]

Keywords: combustion, computational fluid dynamics, flame, modeling, turbulent

1 Introduction

In turbulent combustion, the premixing level between fuel and oxidizer controls the combustion regime that can be premixed or diffusion-controlled. These two regimes exhibit very different flame characteristics. Indeed, while a premixed flame front has a propagation nature, a diffusion flame front cannot propagate and its stabilization is solely controlled by the mixing. Most of the combustion strategies utilize both these combustion regimes exploiting their diverse but complementary characteristics. In particular, the premixed combustion regime boasts an effective control of the emissions, since it allows a direct flame temperature regulation and contains the NO_x formation. In contrast, the diffusion combustion regime is often used to enhance the flame stability. From this perspective, the modeling of multi-regime combustion becomes a strategic element to support the development of novel designs.

Even if the multi-regime combustion is a very common scenario its modeling still represents a challenge [1]. Indeed, the combustion models often rely on "a priori" assumptions regarding the combustion regime, thus limiting their application flexibility. The prediction of multi-regime combustion requires the combustion models to extend their predictivity on widespread conditions and flame configurations. For tabulated chemistry combustion models, several efforts have been made to extend and validate their predictive capabilities to the treatment of multi-regime combustion [2–6]. Nevertheless, using tabulated chemistry becomes increasingly complex when multiple different phenomena have to be accounted for. In particular, in the literature can be found works addressing the inclusion of differential diffusion or flame heat losses, but the simultaneous inclusion of all these aspects in the context of multi-regime combustion is nontrivial. Differently, the thickened flame model for large eddy simulations (TFLES), belonging to the category of the species transport combustion models, includes the heat losses and species differential diffusion even if it has been developed for perfectly premixed conditions. TFLES [7] relies on the artificial thickening of the flame front to allow its resolution on a mesh oriented toward the large eddy simulation (LES) application. The use of the TFLES has become state-of-the-art, especially when H_2 is considered as fuel, thanks to its intrinsic capability to account for the species differential diffusion. Thereafter the original TFLES introduction, a dynamic extension of the model has been proposed for the treatment of the partially premixed combustion. With respect to the original model, the dynamic TFLES (DTFLES) [8] leverages a *flame sensor* Ω for the identification of the flame front where the artificial thickening is applied. Thereby the species and energy diffusivities are altered only in the flame region leaving unaffected the non-reactive mixing. Despite the introduction of this dynamic thickening, the DTFLES is

Turbo Expo, June 24–28, 2024. GT2024.
[1]Corresponding author.
Manuscript received July 9, 2024; final manuscript received July 27, 2024; published online September 5, 2024. Editor: Jerzy T. Sawicki.

still not suitable for modeling multi-regime combustion. Indeed, in the diffusion combustion regime the flame front cannot be thickened as in the premixed one [9], and its treatment must be addressed differently. In this sense, the identification of the local combustion regime becomes pivotal for the proper flame front treatment. To accomplish this task, a local marker known as the *flame index* Ψ is commonly adopted, serving to identify the ongoing combustion regime based on local information. A proper definition of this marker is not a trivial task, as it may be based on gradients alignment [10] or other quantities [11]. Among the flame indices, one of the most widely used is the one proposed by Yamashita et al. [10].

A common strategy to treat the diffusion flame front, whenever it is identified by the flame index, is to disable the thickening leaving its resolution to the local grid [12,13]. Thereby the mesh sizing must ensure a proper discretization of the flame front that requires the use of sufficiently fine grids. Another possibility that allows the relaxation of the static grid refinement requirements is the adoption of a dynamic refinement acting locally on the diffusion flame front [12]. Ultimately, the artificial thickening is inhibited through the flame sensor Ω and the flame index Ψ: while the first one performs a smooth transition when crossing the boundary of the reaction zone [8,14], the second one is generally applied without any regularizations [12].

Anyway, an abrupt change in the thickening entity, ultimately controlled by the thickening factor value F, has an instantaneous effect on the chemical kinetic rates. In contrast, the impact of any diffusivities modification on the flame front thickness requires a characteristic diffusion time to be observed. Thereby, an instantaneous switch in the thickening factor value F could lead to a potential local extinction. Furthermore, numerical discontinuities at the interface between the two flame regimes would be introduced with a direct model application [13]. In order to avoid such undesired effects, this transition of the artificial thickening between premixed and non-premixed regions needs to be numerically smoothed.

In this study, a computationally efficient, smooth dynamic thickening strategy for DTFLES application to multi-regime combustion is proposed and tested against the hydrogen/air flame produced by the HYLON injector [13,15]. The numerical results are compared with detailed experimental data involving reactive and non-reactive particle image velocimetry (PIV), and OH* chemiluminescence measurements. Two different test points have been investigated: in the first one, the flame is anchored and controlled by diffusion, while in the second one the flame is lifted and partially premixed. This second test point exhibits a multi-regime flame stabilization which is particularly interesting for the application of the proposed dynamic model.

The paper is structured as follows: the dynamic thickening strategy is presented in Sec. 2. Then, the test case and the numerical setup are presented in Sec. 3. Cold flow results are shown here in order to validate the setup. In Sec. 4, the results of the application of the thickening strategy to the test case are presented and discussed, along with a comparison to the standard approach for DTFLES in multi-regime combustion. Final considerations are reported in Sec. 5.

2 Dynamic Thickening Strategy

The dynamic thickening strategy for DTFLES application to multi-regime combustion is here presented. Such a model is based on a serial application of cell-based spatial and time regularizations, which evolve based on the quality of local mixing and the grid properties.

Consider a computational cell c at the current time-step t_n, which can be referred to with the superscript $(\cdot)^{[n]}$. By defining a flame index $\Psi^{[n]}(c)$ assuming positive or negative values in cells where premixed or diffusion combustion may occur, respectively, one can determine the local combustion regime in cell c at time-step t_n [12]. In a diffusion flame region no thickening has to be applied, and a local optimal thickening factor $F_{\text{opt},D}$ can be trivially defined for diffusion flames as

$$F^{[n]}_{\text{opt},D}(c) = 1 \tag{1}$$

If this is not the case, premixed combustion is potentially occurring inside cell c at time-step t_n and the optimal thickening factor $F_{\text{opt},P}$ for premixed flames is calculated [8] as

$$F^{[n]}_{\text{opt},P}(c) = 1 + \left[\frac{N\,\Delta x(c)}{\delta^{0\,[n]}_L(c)} - 1\right]\Omega^{[n]}(c) \tag{2}$$

where N is a global user input expressing the required number of grid points inside the flame front in order to accurately integrate the reaction zone when DTFLES is applied, $\Delta x(c)$ expresses the characteristic length of the computational cell c, i.e., the local grid size, and $\delta^{0\,[n]}_L(c)$ expresses the local laminar flame thickness. This last quantity can be sampled in a 1D chemical kinetics solver as a function of the chemical composition and can be imported in the CFD solver through a piecewise polynomial fit. The flame sensor $\Omega^{[n]}(c)$ multiplies the optimal thickening factor to consider a smooth transition to unity when crossing the interface between no flame regions and premixed flame regions, in order to avoid diffusion coefficients modifications in regions where combustion is not occurring. By referring to a global optimal thickening factor $F^{[n]}_{\text{opt}}(c)$, Table 1 summarizes all cases. Variations in F_{opt} can be due to local mixture reactivity, local mixture composition, and local premixing level.

In order to lighten the notation, the reference to the computational cell c is omitted from now on.

2.1 Spatial Smoothing.

With a direct application of the optimal thickening factor $F^{[n]}_{\text{opt}}$, numerical discontinuities persist since the multiplication by Ω in Eq. (2) removes finite jumps between no-flame and premixed flame regions but does not remove internal jumps between diffusion flame and premixed flame regions, as shown in Fig. 1.

A regularization is thus needed leading to the *spatially smoothed thickening factor* F_s

Table 1 Optimal thickening factor

	F_{opt}
Diffusion flame	1
Premixed flame	$1 + \left[\frac{N\,\Delta x}{\delta^0_L} - 1\right]\Omega$

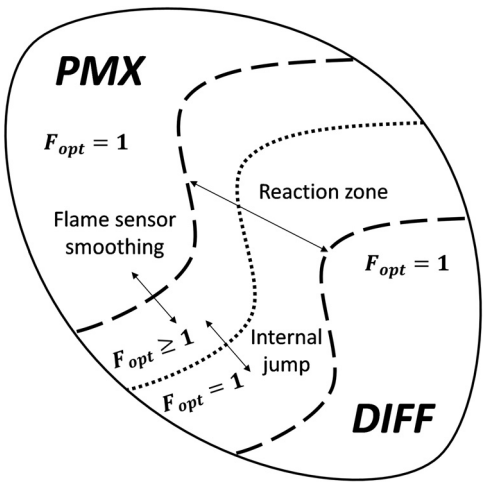

Fig. 1 Multi-regime reaction zone

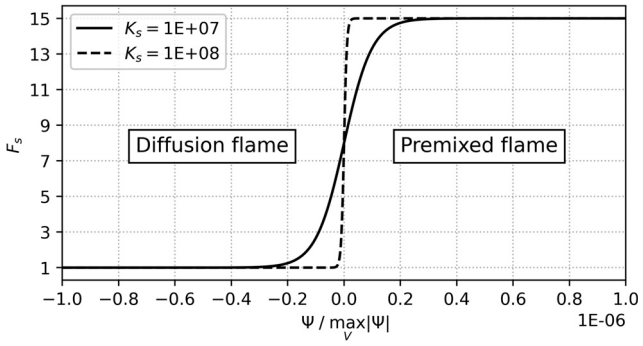

Fig. 2 Regularization of the discontinuity at the interface between premixed and diffusion reaction zones

$$F_s^{[n]} = 1 + \left(F_{\text{opt},P}^{[n]} - 1\right)\left[\frac{1}{2}\left(1 + \tanh\left(K_s \frac{\Psi^{[n]}}{(\max_V|\Psi|)^{[n]}}\right)\right)\right] \quad (3)$$

where V is the computational domain, and K_s is a constant regulating the steepness of the regularization. The square brackets term in the RHS of the equation represents the regularization term for the internal jump in the reaction zone. It is appropriately scaled and adjusted through the other terms in RHS to restore the correct variation limits of the thickening factor. Equation (3) describes a smooth evolution of the thickening factor when crossing the interface separating premixed from diffusion flame regions (Fig. 2). Again, referring to Fig. 1, this regularization has no effect while crossing the interface between no-flame and premixed flame regions since flame index Ψ is always positive, and Ω sensor smoothing is applied instead. The regularization has no effect even crossing the interface between no-flame and diffusion flame regions, since flame index Ψ is always negative and no discontinuities appear.

2.2 Time Smoothing. An example of time regularization for premixed flames is provided in Ref. [16] where a proportional controller continuously measures the gap between the target and the current number of grid elements occupied by the flame front providing corrections to the thickening factor at each time-step.

Following a similar proportional approach, a differential formulation for the regularization in time of the thickening factor evolution is given by the following ordinary differential equation (ODE):

$$\dot{F}(t) = \frac{1}{2}\left[K_{t,P}\,\zeta_+\,(F_{\text{opt},P} - F) + K_{t,D}\,\zeta_-\,(1 - F)\right] \quad (4)$$

where $K_{t,P}$ and $K_{t,D}$ are two constants controlling the evolution speed of the model in the premixed zone and in the diffusion zone, respectively, while

$$\zeta_+ = 1 + \text{sgn}(\Psi), \quad \zeta_- = 1 - \text{sgn}(\Psi) \quad (5)$$

with $\text{sgn}(\cdot)$ referring to the sign function.

Equation (4) relates the time derivative of variable F, which is the thickening factor in the computational cell, with its evolution speed that is proportional to the gaps between the current value of the thickening factor and two optimal target values. The latter are equal to $F_{\text{opt},P}$ for the premixed regime and $F_{\text{opt},D} = 1$ for the diffusion regime, respectively, and are selected according to the value assumed by $\text{sgn}(\Psi)$.

An asymptotic analysis of Eq. (4) leads to multiple equilibrium points uniquely defined by the sign of the flame index. The equilibrium points of the ODE are reported in Table 2. In case of $\Psi = 0$, the model provides a weighted intermediary value between the other two equilibrium points.

Equation (4) is an ODE involving time-dependent variables F, $F_{\text{opt},P}$, and Ψ. Since $F_{\text{opt},P}$ and Ψ are influenced by chemical, convective, and diffusion phenomena, thus by F itself, and vice versa, a fully implicit integration scheme would be required to know $F_{\text{opt},P}^{[n+1]}$ and $\Psi^{[n+1]}$ or to integrate a system with dedicated equations for the three variables accounting for their reciprocal interactions, which are not cell-based. In order to solve the ODE without adding much computational cost, and since an explicit treatment of quantities Ψ and $F_{\text{opt},P}$ ultimately results in a single time-step desynchronization of the equilibrium points, Eq. (4) is integrated through a semi-implicit scheme, meaning that Ψ and $F_{\text{opt},P}$ are evaluated at time-step t_n while calculating $F^{[n+1]}$. This is possible since the quantities $F_{\text{opt},P}$ and Ψ are available from the current CFD solution. Moreover, assuming $F_{\text{opt},P}$ and Ψ as known quantities, Eq. (4) can be treated, at the time-step Δt time scale, as a linear ODE in variable F and the implicit integration can be, for linearity, obtained through a single algebraic calculation involving known variables, without requiring subiterative techniques.

Table 2 Equilibrium points of the ODE

Case	Equilibrium point
$\Psi > 0$	$F \to F_{\text{opt},P}$
$\Psi = 0$	$F \to \dfrac{K_{t,P}F_{\text{opt},P} + K_{t,D}}{K_{t,P} + K_{t,D}}$
$\Psi < 0$	$F \to 1$

Two different linear multi-step formulae (LMF) have been compared for the integration of Eq. (4): the backward Euler formula and the trapezoidal rule. These two implicit schemes are both single-step methods and have different convergence orders and stability properties.

Figure 3 shows the time regularization applied on a computational cell subjected to impulsive changes in combustion regime, chemical reactivity, and composition. While the backward Euler formula shows good results in smoothing the transition to the equilibrium points, the trapezoidal rule suffers from numerical spurious fluctuations. This is essentially due to the absence of the L-stability property in the trapezoidal rule.

To avoid such fluctuations which lead to high overestimations and underestimations in the numerical solution of the ODE, and in order

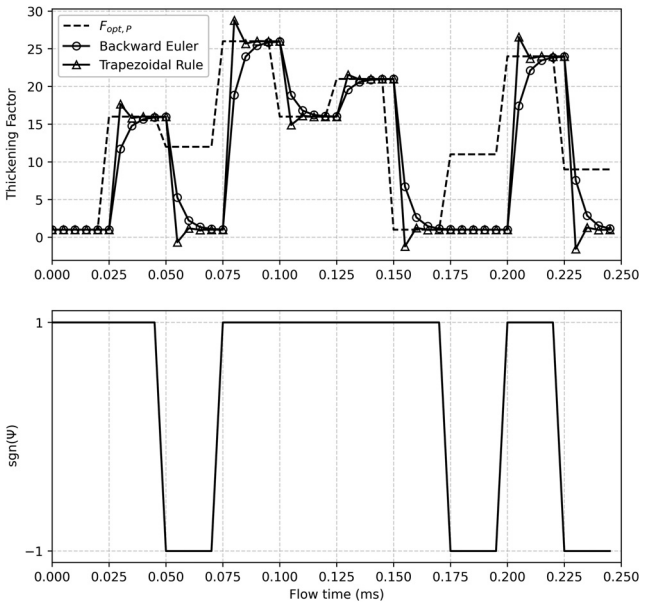

Fig. 3 Simulation of the time smoothing strategy on a fixed computational cell and comparison between the considered semi-implicit integration schemes (top). Combustion regime detected by the flame index (bottom).

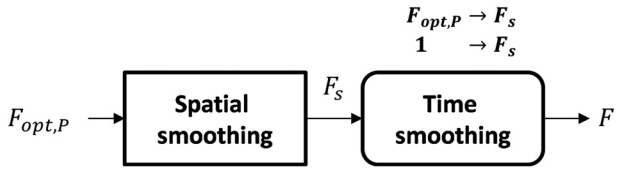

Fig. 4 Combined regularization in space and time

to ensure a smooth solution, the backward Euler formula has been finally chosen for the numerical integration of Eq. (4). This is achieved through the following algebraic expression, which only makes use of available quantities:

$$F^{[n+1]} = \frac{F^{[n]} + \frac{\Delta t}{2}\left(K_{t,P}\,\zeta_+^{[n]} F_{\text{opt},P}^{[n]} + K_{t,D}\,\zeta_-^{[n]}\right)}{1 + \frac{\Delta t}{2}\left(K_{t,P}\,\zeta_+^{[n]} + K_{t,D}\,\zeta_-^{[n]}\right)} \tag{6}$$

where Δt is the time-step size and

$$\zeta_+^{[n]} = 1 + \text{sgn}(\Psi^{[n]}), \quad \zeta_-^{[n]} = 1 - \text{sgn}(\Psi^{[n]}) \tag{7}$$

2.3 Combined Smoothing. The two complementary approaches can be combined to obtain a regularization in both space and time. This can be achieved by simply substituting terms $F_{\text{opt},P}$ and 1 in Eq. (4), corresponding to the premixed and diffusion equilibrium points, with term F_s obtained through the spatial smoothing, as reported in Fig. 4.

This way, the number of equilibrium points reduces from three to only one, corresponding to value F_s.

The numerical regularized solution can be calculated as

$$F^{[n+1]} = \frac{F^{[n]} + \frac{\Delta t}{2} F_s^{[n]}\left(K_{t,P}\,\zeta_+^{[n]} + K_{t,D}\,\zeta_-^{[n]}\right)}{1 + \frac{\Delta t}{2}\left(K_{t,P}\,\zeta_+^{[n]} + K_{t,D}\,\zeta_-^{[n]}\right)} \tag{8}$$

Before its application, the updated thickening factor is filtered through the sensor Ω as in Eq. (2) in order to avoid modifications of the diffusivities out of the flame region.

Note that the regularization does not depend on the specific definitions of sensor Ω and flame index Ψ. Only a continuous variation of the latter is required for the spatial regularization.

3 Test Case and Numerical Setup

The proposed regularization has been implemented in the commercial solver ANSYS FLUENT 2023 R1 through *user defined functions* (UDFs) and it has been tested against a multi-regime combustion burner. The individuated test case is the hydrogen/air flame produced by the dual-swirl coaxial HYLON (HYdrogen LOw-NO_x) injector [13,15] which, showing multi-regime combustion and different stabilization regimes, has been individuated as an interesting benchmark for the presented dynamic model.

Anyway, a proper validation of the model may require investigations on a different test case characterized by more complex features of the combustion regime. A comparison between the standard DTFLES model and the proposed regularized model is reported in Sec. 4.

Geometrical details about the injector and the combustion chamber, together with the experimental results from Institut de Mécanique des Fluides de Toulouse (IMFT), are available for two different operating points [15] named flames A (attached) and L (lifted), respectively. The version of the database used for comparisons is HYLON_TNF_2023_04, updated on April 2023. For both flames, the burner is operated in very lean conditions with a global equivalence ratio $\phi_g = 0.45$ and reactants are injected separately through coaxial channels. The two flames differ in reactants mass flow rates and, thus, in thermal power. For flame A, the burner is operated at 3.89 kW and a triple flame is able to propagate along isosurfaces of stoichiometric mixture fraction Z_{st} since flow velocities are smaller than the triple flame propagation speed S_d, leading to a flame configuration attached to the injector. For flame L, the burner is operated at 9.73 kW and flow velocities are higher than S_d, leading to a flame liftoff and, thus, a different stabilization regime [17–19].

Table 3 Operating conditions for flames A and L

Case	$\dot{m}_{\text{air}}$ (g/s)	$\dot{m}_{H_2}$ (g/s)	p_{op} (Pa)	T_u (K)	P_{th} (kW)	ϕ_g
A	2.41	0.032	101325	298	3.89	0.45
L	6.03	0.080	101325	298	9.73	0.45

Table 3 summarizes operating conditions for flames A and L.

Both flames have been investigated through high-fidelity LES analyses, for cold and reactive flow conditions.

In this section, the numerical setup is presented and only cold flow results are shown in order to first validate the adopted numerical grid and the turbulence model. Following a previous work [13], a mesh with dedicated refinements in regions interested by non-premixed combustion has been considered. Furthermore, the domain has been extended by including a downstream hemisphere to dampen pressure fluctuations. The grid accounts for 18.6 million polyhedral and prismatic cells.

Figure 5 shows details of the burner geometry, the combustion chamber, the downstream hemispherical extension, and the numerical grid, while in Table 4 the grid sizings are reported.

Cold and reactive flow LES calculations of both flames A and L have been run on ANSYS FLUENT 2023 R1 with the pressure-based solver, by adopting a constant time-step size $\Delta t = 5 \times 10^{-6}$ s and by performing a constant number of 10 subiterations inside each time-step. In order to handle statistically converged solutions, all the

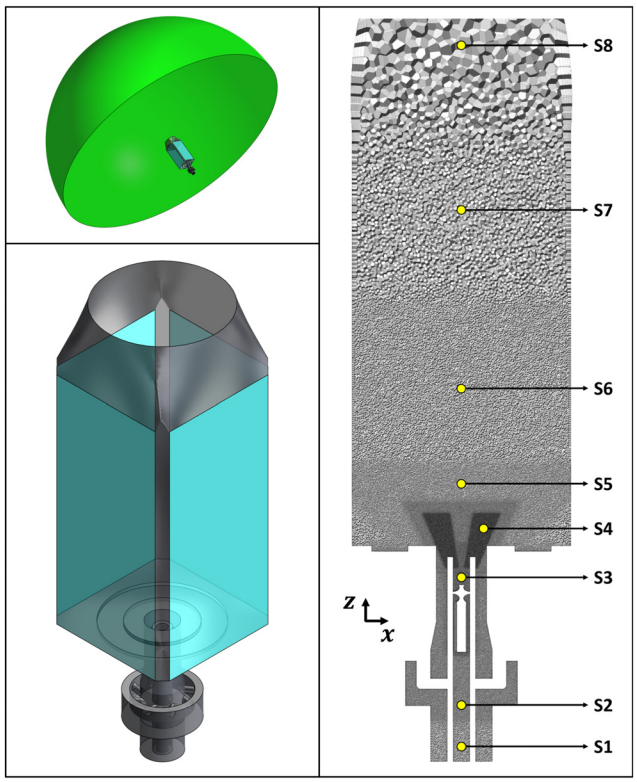

Fig. 5 Extension of the geometry with a hemisphere (top left). Geometry of the burner and combustion chamber (bottom left). Numerical grid (right).

Table 4 Numerical grid sizings

	S1	S2	S3	S4	S5	S6	S7	S8
(mm)	0.50	0.30	0.15	0.10	0.40	0.70	1.50	5.00

simulations have been flushed for a sufficient amount of time, and then statistics have been collected. The Smagorinsky-Lilly model with dynamic stresses [20–22] has been chosen as subgrid-scale turbulent closure for the momentum equation. Chemical kinetics and species transport rely on the skeletal Boivin mechanism [23] comprising 8 species and 12 reactions, together with the addition of molecular nitrogen whose properties were imported from the UCSD detailed mechanism [24]. The species laminar diffusion coefficients have been calculated with the mixture-averaged diffusion model. In cold flow conditions, all the walls have been considered adiabatic walls, while in reactive flow conditions, a heat loss has been considered by imposing the experimental temperature profiles available in Ref. [15] as boundary conditions on the fused silica walls, the metallic pillars walls, and the nozzle walls. Since thermocouples on fused silica walls and stainless steel pillars have been applied on the cold side for the measurements, a 1D steady heat conduction equation is solved in those cases to account for a wall thickness, and the temperature profile is imposed on a virtual 1D extrusion of the wall. For the fused silica, a thermal conductivity $\lambda^{\text{fs}} = 2.07\,\text{Wm}^{-1}\text{K}^{-1}$, a specific heat $C_p^{\text{fs}} = 1214\,\text{JKg}^{-1}\text{K}^{-1}$, and a thickness $l^{\text{fs}} = 8$ mm have been considered, while for the stainless steel such properties have been setup as $\lambda^{\text{ss}} = 20.66\,\text{Wm}^{-1}\text{K}^{-1}$, $C_p^{\text{ss}} = 581\,\text{JKg}^{-1}\text{K}^{-1}$, and $l^{\text{ss}} = 11.8$ mm. On the backplate, a constant temperature of 450 K has been applied in reactive flow conditions as in Ref. [13]. For the momentum equation, the no-slip condition has been applied on all the physical walls, while a free-slip condition has been imposed on the bottom wall of the hemispherical extension. The mass flow rates and fresh gases temperature indicated in Table 3 have been imposed at the air and hydrogen coaxial inlet channels, respectively, while the operating pressure has been imposed on the top surface of the hemisphere, which has been considered the outlet.

Cold flow simulations have been performed by solving both air and hydrogen diffusion-transport equations. For this reason, the numerical cold flow results can be directly compared with the experimental ones available in Ref. [15].

Perfect reactants mixing at fresh gases temperature T_u and global equivalence ratio ϕ_g have been imposed as an outlet boundary condition to handle potential backflow in cold flow simulations, while chemical equilibrium backflow temperature and composition have been imposed in reactive flow simulations, for the same reason.

Laminar flame properties have been sampled by solving 1D freely propagating flames in Cantera [25] and they have been imported in the commercial solver through a fit by making use of piecewise polynomial functions.

A user input of $N = 10$ grid points inside the flame front has been chosen in reactive flow simulations, meaning that the $F^{[n]}_{\text{opt},P}(c)$, which is automatically calculated by the solver when the thickened flame model is enabled, is asked to reach this requirement.

Since the flow is turbulent, also a model to recover turbulence-chemistry interactions is needed. The subgrid efficiency model presented in Ref. [7], with the formulation for unstructured grids discussed in Ref. [26], has been adopted in reactive flow simulations.

The dynamic thickening strategy presented in Sec. 2 has been applied to reactive simulations of both flames A and L with constants $K_s = 1 \times 10^7$, and $K_{t,P} = K_{t,D} = 2 \times 10^5\ \text{s}^{-1}$.

The choice of the latter two has been based on a sensitivity analysis and will be discussed in Sec. 4.

Since the model does not explicitly depend on the definitions of the flame sensor Ω and flame index Ψ, a clarification on which quantities have been used is necessary. Regarding the flame sensor Ω, the default model implemented in the commercial CFD solver has been adopted, whose definition relies on [8]

$$\Omega^{[n]} = \tanh\left(10\,\frac{\overline{|R|}^{[n]}}{\left(\max_V \overline{|R|}\right)^{[n]}}\right) \tag{9}$$

with $\overline{|R|}$ the spatially filtered absolute value of the reaction rate.

Regarding the choice of the flame index Ψ, it is required to assume positive or negative values where premixed or diffusion combustion occurs, respectively. The Takeno index with molecular hydrogen as fuel and molecular oxygen as oxidizer [10] has been chosen for such purpose

$$\Psi^{[n]} = \nabla Y^{[n]}_{\text{H}_2} \cdot \nabla Y^{[n]}_{\text{O}_2} \tag{10}$$

3.1 Cold Flow Results. Figures 6 and 7 report the axial and radial velocity profiles on different axial planes for cold flow conditions of flame A and flame L, respectively, both in terms of mean values and root-mean-square (rms) fluctuations. Experimental data was linearly interpolated by the PIV measurements available in the database [15], while numerical data was extracted on the XZ plane. Both have been evaluated on isolines defined by $y = 0$ mm and $z = 5$ mm, $z = 10$ mm, $z = 15$ mm, and $z = 20$ mm, respectively.

The peaks of both axial and radial velocities immediately downstream of the swirlers are well captured, meaning that the numerical model correctly characterizes the internal and external shear layers which could play a key role in flame stabilization during the subsequent reactive simulations.

Moving along the axial direction, the inner recirculation zone (IRZ) is well reconstructed, even if a slight overestimation of the IRZ intensity is visible in Fig. 6 for flame A, and in Fig. 7 for flame L, especially at $z \leq 10$ mm.

The goodness of the numerical model is underlined by the prediction of the rms fluctuations, which confirms a correct characterization of the local turbulence intensity.

Figures 8 and 9 report the same velocity and fluctuations components through contour plots whose radial and axial limits coincide with the experimental PIV validity ranges indicated in Ref. [15]. This allows a direct comparison between the experimental PIV measurements and the numerical results extracted on the same plane.

The agreement between experimental and numerical results is confirmed, leading to the conclusion that the numerical model is able to predict correctly the cold aerodynamic flow fields for both flames

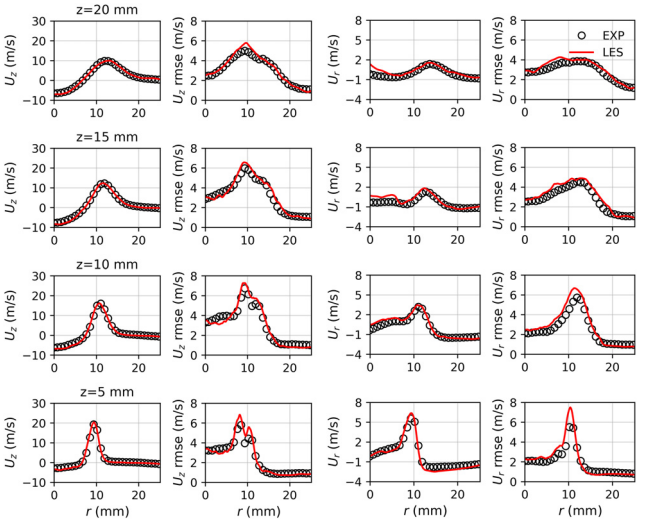

Fig. 6 Mean and rms velocity profiles for flame A—cold flow on different axial planes

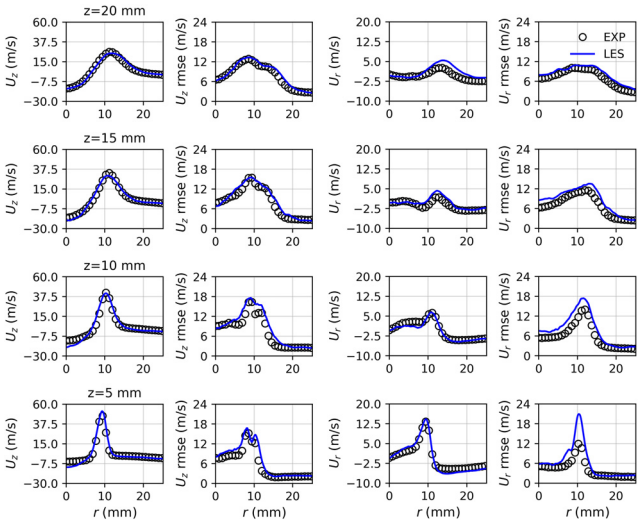

Fig. 7 Mean and rms velocity profiles for flame L—cold flow on different axial planes

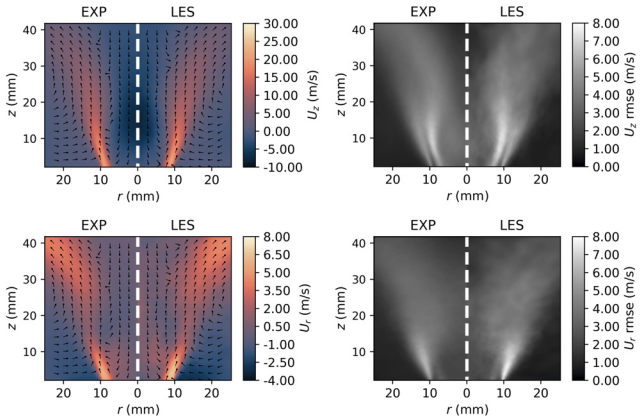

Fig. 8 Comparison between experimental PIV and numerical results for flame A—cold flow

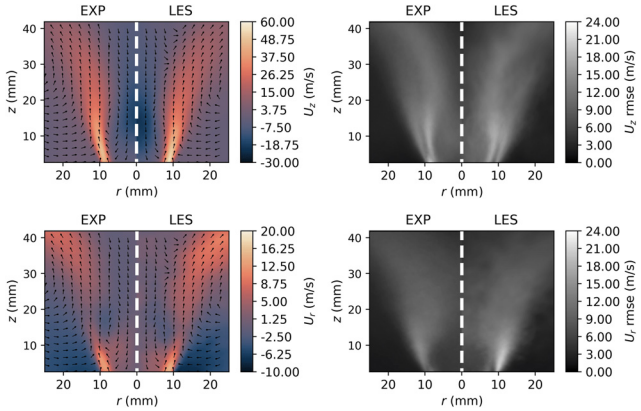

Fig. 9 Comparison between experimental PIV and numerical results for flame L—cold flow

A and L. A numerical overestimation in radial velocity rms fluctuations can be observed near the backplate, at $z \leq 10$ mm. Anyway, the agreement between the numerical and experimental decay of fluctuations at $z > 10$ mm suggests a correct prediction in the growth and decay of the turbulent eddies.

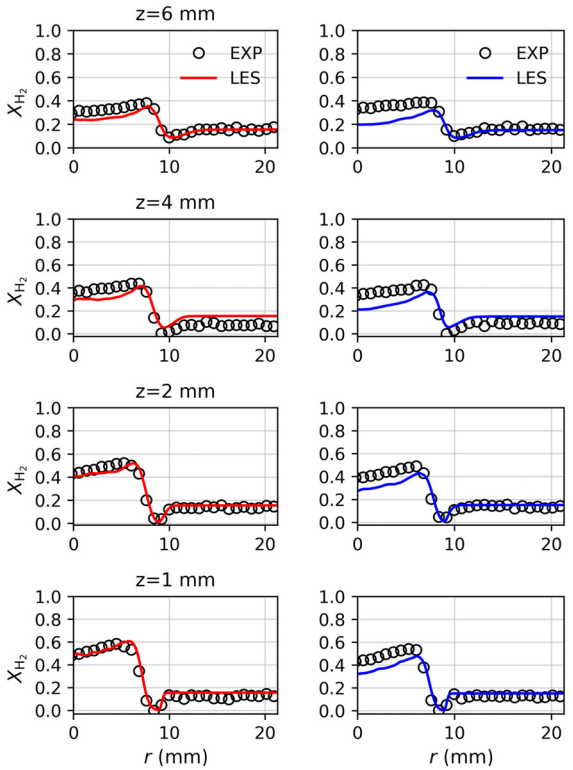

Fig. 10 Cold flow comparison of hydrogen molar fractions in flame A (left) and flame L (right)

Figure 10 reports a comparison between experimental and numerical results in terms of cold flow hydrogen molar fraction distribution. Again, the peaks and the maximum and minimum points are well predicted by the numerical model. While for flame A (left, red) the agreement over the entire radial distribution is almost perfect on all axial planes, for flame L (right, blue) the distribution along the z axis at $r = 0$ mm is slightly underestimated. This could be due to the numerical overestimation of the IRZ intensity.

Experimental and numerical cold flow results are in good agreement: the adopted numerical model correctly predicts the aerodynamic fields and the species diffusion in the combustion chamber for both flames A and L, thus it can be validated.

4 Application of the Thickening Strategy in Reactive Flow Conditions

Figures 11 and 12 show the comparison between experimental data and numerical results for the axial and radial velocity components on different axial planes for flames A and L in reactive flow conditions, both in terms of mean values and rms fluctuations. The agreement between experimental and numerical results is very good and, as for cold flow conditions, the peak values and their locations are correctly predicted by the numerical model for axial and radial velocity components.

Again, the model is able to predict the peak values downstream of the swirler and the axial decay of the rms fluctuations, proving to be capable of an accurate reconstruction of both the reactive flow field and the turbulent eddies evolution, a fundamental requirement in order to preserve the accuracy of the subgrid efficiency model.

On flame L, the numerical peaks of rms fluctuations of axial velocity are reached at a slightly smaller radial coordinate on the axial plane $z = 20$ mm, with respect to experimental results. Furthermore, a small overestimation of the IRZ intensity is confirmed on flame A and flame L, especially for $z \leq 5$ mm.

Figures 13 and 14 show the reactive aerodynamic flow field through contour plots whose radial and axial limits again coincide with the validity ranges of the experimental PIV data. The smaller

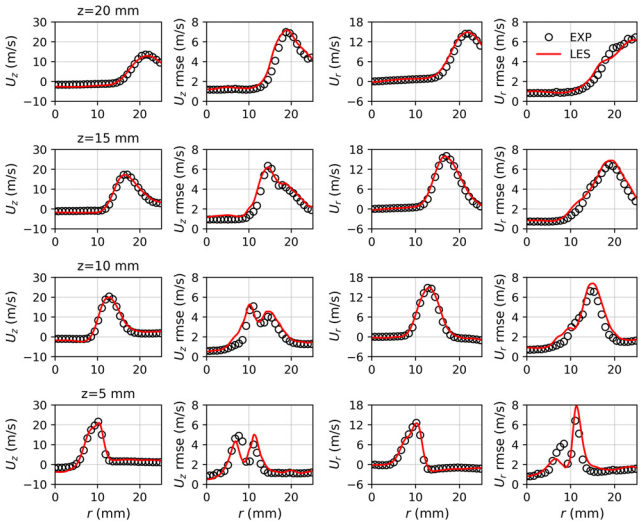

Fig. 11 Mean and rms velocity profiles for flame A—reactive flow on different axial planes

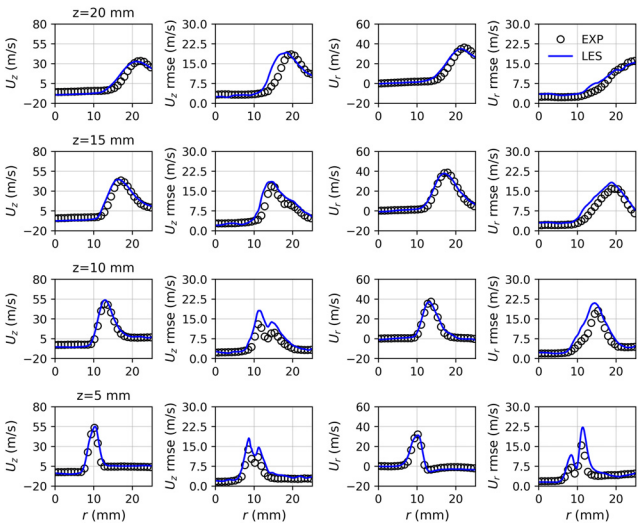

Fig. 12 Mean and rms velocity profiles for flame L—reactive flow on different axial planes

radial coordinate at which peaks of the numerical fluctuation of the axial velocity is here visible in terms of a lower opening angle with respect to the z axis individuated by $r = 0$ mm.

Figure 15 shows the comparison between the Abel-deconvoluted OH* chemiluminescence measurements available in Ref. [15] and the numerical prediction of the normalized mean heat release rate for both flames A and L. A portion of the left part of the two subfigures is hidden since no experimental optical access is available below the backplate. Flame A (left) stabilizes attached to the injector assuming an M-shape. A peak in heat release rate distribution associated with a diffusion flame front is observed along the mixing layer, characterized by high levels of strain and scalar dissipation rate, downstream of the coaxial channels. A secondary, weaker, diffusion flame front develops downstream of the first one. In contrast, flame L (right) aerodynamically stabilizes lifted above the injector assuming a V-shape and ensuring a higher degree of mixing between fresh reactants. Indeed, the main peak of heat release rate distribution is associated with a partially premixed flame front, even if a secondary diffusion frame front is still present. The two flames have been well reconstructed by the numerical model, as confirmed by the comparison shown in Fig. 15.

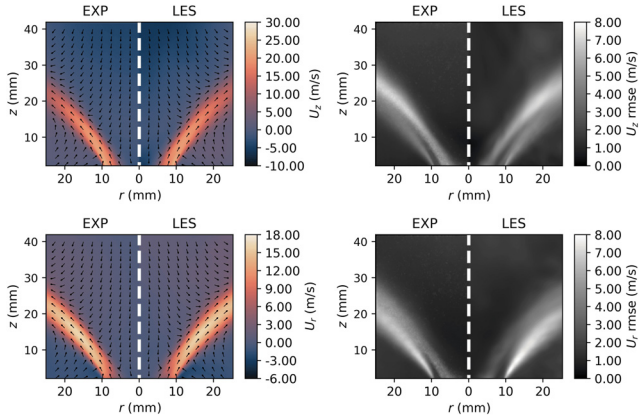

Fig. 13 Comparison between experimental PIV and numerical results for flame A—reactive flow

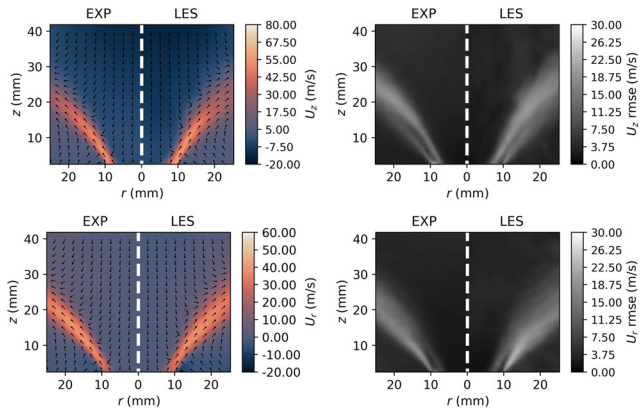

Fig. 14 Comparison between experimental PIV and numerical results for flame L—reactive flow

Figures 16 and 17 show the instantaneous behavior of the model on flames A and L, respectively. Isolines of normalized heat release rate $\mathrm{HRR}_{\mathrm{norm}} = 0.15$ are plotted with red solid lines, while isolines of stoichiometric mixture fraction $Z = Z_{\mathrm{st}}$ are plotted with white solid lines. Referring to Fig. 16, in flame A the heat release rate is concentrated along the isoline of stoichiometric mixture fraction and the flame front is dominated by species diffusion.

Due to the diffusion flame regime, here the instantaneous spatial regularization based on the flame index Ψ does not predict the need for an artificial thickening, meaning that $F_s = 1$. Accordingly, since the target value to reach in the time regularization is unitary, no effective artificial thickening is applied, leading to $F = 1$.

Referring instead to Fig. 17, in flame L the main reaction zone is characterized by partially premixed combustion, since a portion of the flame front develops in a diffusion regime while another one develops

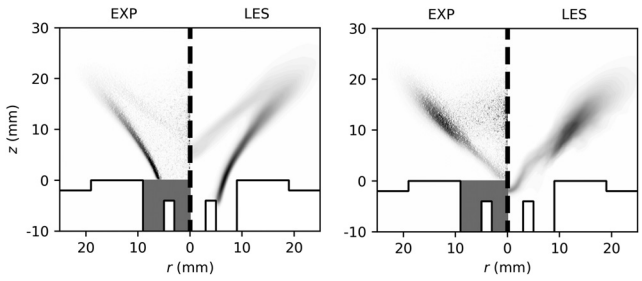

Fig. 15 Comparison between experimental OH* chemiluminescence measurements and numerical normalized mean heat release rate for flame A (left) and flame L (right)

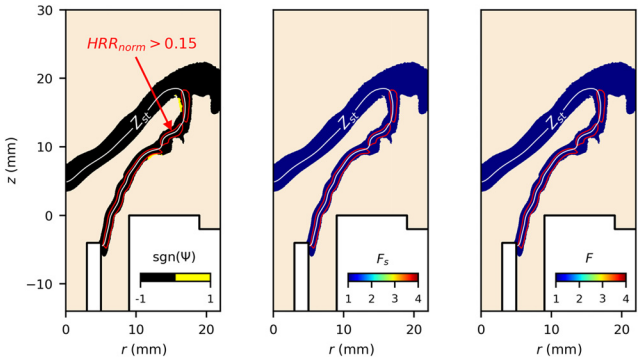

Fig. 16 Instantaneous behavior of the model on flame A. Isolines of normalized heat release rate HRR_{norm} and isolines of stoichiometric mixture fraction Z_{st} (solid lines). Combustion regime detected by the flame index (left). Target spatially smoothed thickening factor (center). Applied thickening factor (right).

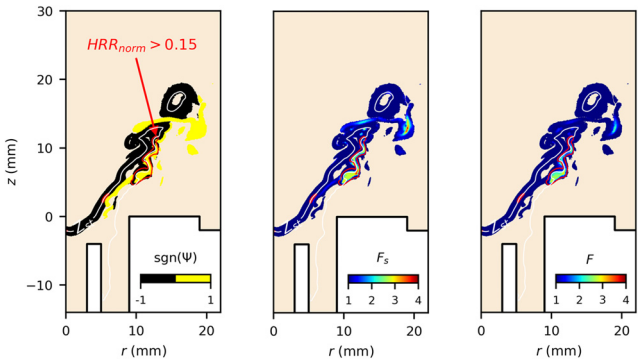

Fig. 17 Instantaneous behavior of the model on flame L. Isolines of normalized heat release rate HRR_{norm} and isolines of stoichiometric mixture fraction Z_{st} (solid lines). Combustion regime detected by the flame index (left). Target spatially smoothed thickening factor (center). Applied thickening factor (right).

in a premixed regime. Here, the instantaneous spatial regularization predicts the need for an artificial thickening, leading to an effective distribution of the F_s values according to the combustion regime, the chemical reactivity, and the local mixture composition. Accordingly, the effective thickening factor to be applied evolves in time, being able to regularize the thickening factor dynamics while reaching comparable values with the spatially smoothed target F_s.

Figure 18 shows the results of a sensitivity analysis of the model on different values of the constants $K_{t,P}$ and $K_{t,D}$ in a fixed computational cell c located in a region statistically interested by the flame front. The analysis has been performed through reactive calculations of flame L in order to individuate potential appropriate ranges of the model constants. $K_{t,P}$ and $K_{t,D}$ were varied together while assuming specular values during the tests, meaning that the effects provided by an imbalance in the model evolution rates between premixed and diffusion combustion zones have not been investigated. It has been observed that for values below 1×10^5 s^{-1} the model evolves too slowly and it is not able to reach the same peaks of the target value F_s. On the other side, for values over 5×10^5 s^{-1} the model is very responsive and F_s peaks are well captured in that case. Anyway, the finite jumps of the thickening factor F between two consecutive time steps start to be comparable with the ones of the instantaneous spatially smoothed target F_s, leading to a potential loss of benefit from the time regularization provided by the model. Based on these considerations, the values $K_{t,P} = K_{t,D} = 2 \times 10^5$ s^{-1} have been chosen to perform the reactive flow simulations of both flames, as indicated in Sec. 3.

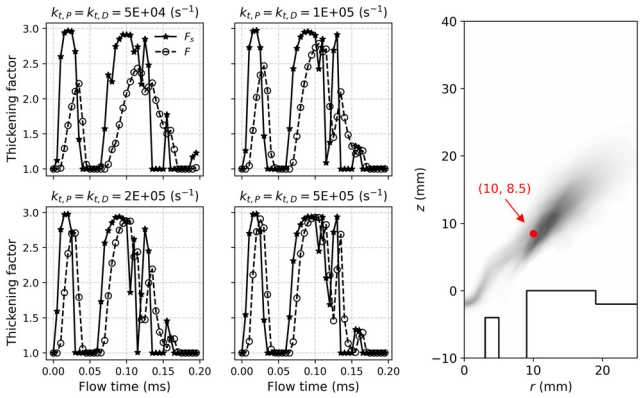

Fig. 18 Sensitivity analysis of the model on different values of the constants $K_{t,P}$ and $K_{t,D}$ in a fixed computational cell c (left). Location of the cell c (right).

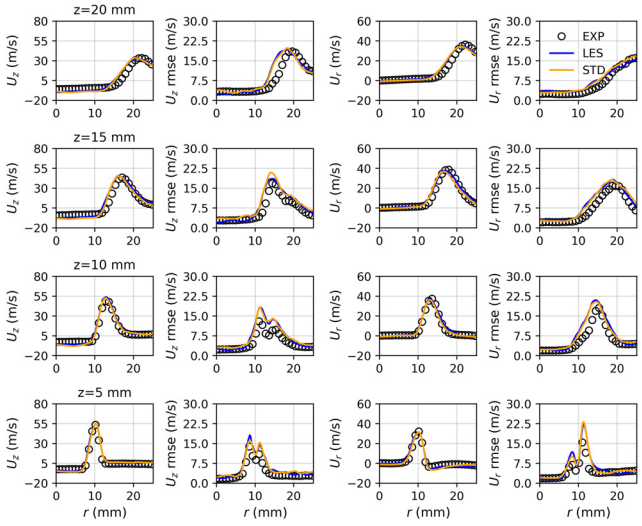

Fig. 19 Comparison between the proposed model and the standard approach in terms of mean and rms velocity profiles for flame L—reactive flow. Experimental data (circles). Profiles obtained with the proposed model and with the standard approach (solid lines).

4.1 Comparison With the Standard Approach. To assess the impact of the proposed model, LES reactive flow simulations of flame L were conducted again with the smoothing strategy disabled, instead adopting the standard DTFLES approach for multi-regime combustion. The flame index Ψ is used to activate the thickening only on premixed flame fronts. Neither spatial regularization at the interface between premixed and diffusion regimes on the front, nor time regularization were applied. The smooth transition to a unitary thickening factor provided by the flame sensor Ω between flame and no flame regions is an integral aspect of the DTFLES model and it was preserved, along with the rest of the numerical setup.

Figure 19 reports the comparison between the prediction of velocity fields with the proposed model (solid blue line) and with the standard DTFLES, flame index controlled model (solid orange line). To preserve the notation, the proposed model is again labeled LES, while the standard model is labeled STD. Both predictions are compared with experimental data (black circles). Numerical results are very similar and accurate in both cases. Some discrepancies can be observed in mean axial velocity profiles, with the standard DTFLES predicting a slightly lower axial velocity at $r = 0$ mm across all reported axial coordinates, and a lower axial velocity at $z = 15$ mm, for $r > 15$ mm. The peak of axial velocity fluctuations is closer to the

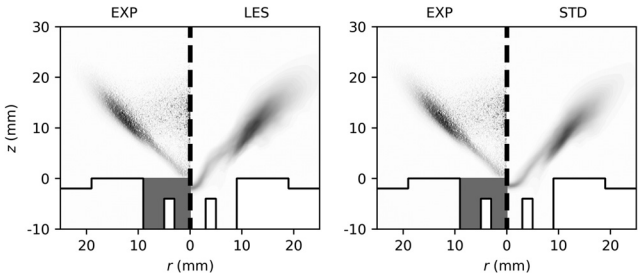

Fig. 20 Comparison between experimental OH* chemiluminescence measurements and numerical normalized mean heat release rate with the proposed model (left) and the standard approach (right)

experimental data with the standard DTFLES model at $z = 5$ mm, while at $z = 15$ mm it is better predicted by the proposed model. Axial velocity fluctuations around $r = 0$ mm are greater with the standard DTFLES with respect to the predictions of the proposed model.

Even if predictions of mean radial velocity are quite similar, a slight underestimation can be observed at $z = 15$ mm, for $r > 15$ mm, with the standard DTFLES model. The peak in radial velocity fluctuations at $z = 5$ mm, for $r < 10$ mm, is slightly closer to the experimental results with the standard DTFLES model compared to the proposed one, which, instead, better predicts radial velocity fluctuations at $r > 15$ mm across all reported axial coordinates. Both strategies predict the velocity fields with a high level of accuracy.

Figure 20 shows the comparison between the experimental OH* chemiluminescence measurements and the numerical normalized mean heat release rate with the proposed model (left side of the figure) and the standard DTFLES model (right side of the figure). The notation of Fig. 19 is maintained. The V-shape of the lifted flame is recovered with both models. The zone where the maximum values of the time-averaged heat release rate are reached is slightly thinner in the case of the standard model. The lift-off height predicted by the standard DTFLES is slightly lower than the one predicted by the proposed model.

The comparison has shown minimal differences between the results provided by the two models. Indeed, the benefits provided by the regularization of the thickening factor don't seem to have a significant impact on the HYLON flame L atmospheric test case. A greater impact is expected when variations in the thickening factor values become larger, for example, at higher pressure, when the laminar flame front becomes thinner with respect to the numerical grid size.

5 Conclusion

In this study, a dynamic thickening strategy for DTFLES application to high-fidelity CFD analyses of multi-regime combustion has been proposed. The strategy leads to a regularization of the thickening factor evolution in the computational cell c in both space and time, and the intensity of the regularization can be controlled by means of three different model constants. The model has been tested on the hydrogen/air flame produced by the HYLON injector, which naturally exhibits multi-regime combustion, showing promising results. Indeed, the differences between the experimental results from IMFT and the obtained numerical results are very small, and the two flames have been correctly predicted by the proposed model both in terms of velocity components and heat release rate distribution.

In the numerical simulations, the model constants were chosen after a dedicated sensitivity analysis. The chosen values are not universal and, since no additional scalar equations are introduced by the regularization, an appropriate evolution speed of this cell-based model could be based both on convection and diffusion characteristic time scales.

The regularization extends the DTFLES application to multi-regime combustion analyses.

Since the model does not make assumptions neither about the operating pressure nor about the temperature of the fresh reactants, it can be used for numerical analyses on industrial burners.

The regularization makes no assumption even about the definitions of the flame sensor Ω and flame index Ψ, except for a continuous variation of the latter which is exploited during the spatial smoothing phase, thus the model can be used also in combination with more refined formulations of these two indices, with respect to the ones chosen in this work.

A comparison between the proposed regularized model and the standard approach for the adoption of the DTFLES model in multi-regime combustion was performed on the HYLON flame L atmospheric test case, showing minimal differences in numerical results. The model will be tested in future works at higher pressure, where a greater impact of the proposed regularization is expected.

Acknowledgment

The authors would like to acknowledge Thierry Schuller, IMFT (Toulouse) for sharing the experimental data used in this work.

Nomenclature

Roman Letters

C = specific heat (J kg^{-1} K^{-1})
D = diffusivity (m^2 s^{-1})
F = thickening factor
$\dot{m}$ = mass flow rate (g s^{-1})
N = grid points in flame front
p = pressure (Pa)
P = power (kW)
R = reaction rate (kmol m^{-3} s^{-1})
s = flame speed (m s^{-1})
U = velocity (m s^{-1})
X = mole fraction
Y = mass fraction
Z = mixture fraction

Greek Symbols

δ = flame thickness (m)
Δt = time step size (s)
Δx = numerical grid size (m)
λ = thermal conductivity (W m^{-1} K^{-1})
ϕ = equivalence ratio
Ψ = flame index (m^{-2})
Ω = flame sensor

Superscripts and Subscripts

air = air
D = diffusion flame
fs = fused silica
g = global
H_2 = hydrogen
L = laminar
n = value at time step t_n
$n+1$ = value at time step t_{n+1}
op = operating
opt = optimal
p = constant pressure
P = premixed flame
r = radial
s = spatial smoothing
ss = stainless steel
st = stoichiometric
t = time smoothing
th = thermal
u = fresh gases

z = axial
0 = thin flame

References

[1] Fiorina, B., Luu, T. P., Dillon, S., Mercier, R., Wang, P., Angelilli, L., Ciottoli, P. P., et al., 2023, "A Joint Numerical Study of Multi-Regime Turbulent Combustion," Appl. Energy Combust. Sci., **16**, p. 100221.

[2] Knudsen, E., and Pitsch, H., 2012, "Capabilities and Limitations of Multi-Regime Flamelet Combustion Models," Combust. Flame, **159**(1), pp. 242–264.

[3] Zhang, W., Han, W., Wang, J., Huang, Z., Jin, W., and van Oijen, J., 2023, "Large-Eddy Simulation of the Darmstadt Multi-Regime Turbulent Flame Using Flamelet-Generated Manifolds," Combust. Flame, **257**, p. 113001.

[4] Langella, I., Swaminathan, N., and Pitz, R. W., 2016, "Application of Unstrained Flamelet SGS Closure for Multi-Regime Premixed Combustion," Combust. Flame, **173**, pp. 161–178.

[5] Massey, J. C., Li, Z., Chen, Z. X., Tanaka, Y., and Swaminathan, N., 2023, "Large Eddy Simulation of Multi-Regime Combustion With a Two-Progress Variable Approach for Carbon Monoxide," Proc. Combust. Inst., **39**(2), pp. 2117–2127.

[6] Engelmann, L., Wollny, P., Breicher, A., Geyer, D., Chakraborty, N., and Kempf, A., 2023, "Numerical Analysis of Multi-Regime Combustion Using Flamelet Generated Manifolds - A Highly-Resolved Large-Eddy Simulation of the Darmstadt Multi-Regime Burner," Combust. Flame, **251**, p. 112718.

[7] Colin, O., Ducros, F., Veynante, D., and Poinsot, T., 2000, "A Thickened Flame Model for Large Eddy Simulations of Turbulent Premixed Combustion," Phys. Fluids, **12**(7), pp. 1843–1863.

[8] Legier, J. P., Poinsot, T., and Veynante, D., 2000, "Dynamically Thickened Flame LES Model for Premixed and Non-Premixed Turbulent Combustion," Proceedings of the Summer Program, Centre for Turbulence Research, Stanford, CA, Nov., pp. 157–168.

[9] Cuenot, B., Shum-Kivan, F., and Blanchard, S., 2022, "The Thickened Flame Approach for Non-Premixed Combustion: Principles and Implications for Turbulent Combustion Modeling," Combust. Flame, **239**, p. 111702.

[10] Yamashita, H., Shimada, M., and Takeno, T., 1996, "A Numerical Study on Flame Stability at the Transition Point of Jet Diffusion Flames," Symp. (Int.) Combust., **26**(1), pp. 27–34.

[11] Zirwes, T., Zhang, F., Habisreuther, P., Hansinger, M., Bockhorn, H., Pfitzner, M., and Trimis, D., 2021, "Identification of Flame Regimes in Partially Premixed Combustion From a Quasi-DNS Dataset," Flow, Turbul. Combust., (**106**(2), pp. 373–404.

[12] Castellani, S., Meloni, R., Orsino, S., Ansari, N., Yadav, R., Bessette, D., Boxx, I., and Andreini, A., 2023, "High-Fidelity H_2–CH_4 Jet in Crossflow Modelling With a Flame Index-Controlled Artificially Thickened Flame Model," Int. J. Hydrogen Energy, **48**(90), pp. 35291–35304.

[13] Aniello, A., Laera, D., Marragou, S., Magnes, H., Selle, L., Schuller, T., and Poinsot, T., 2023, "Experimental and Numerical Investigation of Two Flame Stabilization Regimes Observed in a Dual Swirl H2-Air Coaxial Injector," Combust. Flame, **249**, p. 112595.

[14] Jaravel, T., 2016, "Prediction of Pollutants in Gas Turbines Using Large Eddy Simulation," Ph.D. thesis, Institut National Polytechnique de Toulouse, Toulouse, France.

[15] Vilespy, M., Marragou, S., Magnes, H., Aniello, A., Selle, L., Poinsot, T., and Schuller, T., 2023, "Measurements Dataset of Hydrogen/Air Flames in a Dual Swirl Coaxial Injector," TNF Workshop, accessed Aug. 22, 2024, https://tnfworkshop.org/hylon-hydrogen-air-flames-in-a-dual-swirl-coaxial-injector-imft-toulouse/

[16] Rochette, B., Riber, E., Cuenot, B., and Vermorel, O., 2020, "A Generic and Self-Adapting Method for Flame Detection and Thickening in the Thickened Flame Model," Combust. Flame, **212**, pp. 448–458.

[17] Marragou, S., Magnes, H., Aniello, A., Selle, L., Poinsot, T., and Schuller, T., 2023, "Experimental Analysis and Theoretical Lift-Off Criterion for H_2/Air Flames Stabilized on a Dual Swirl Injector," Proc. Combust. Inst., **39**(4), pp. 4345–4354.

[18] Marragou, S., Magnes, H., Aniello, A., Guiberti, T., Selle, L., Poinsot, T., and Schuller, T., 2023, "Modeling of H_2/Air Flame Stabilization Regime Above Coaxial Dual Swirl Injectors," Combust. Flame, **255**, p. 112908.

[19] Magnes, H., Marragou, S., Aniello, A., Selle, L., Poinsot, T., and Schuller, T., 2023, "Impact of Preheating on Flame Stabilization and NOx Emissions From a Dual Swirl Hydrogen Injector," ASME J. Eng. Gas Turbines Power, **146**(5), p. 051004.

[20] Smagorinsky, J., 1963, "General Circulation Experiments With the Primitive Equations: I–The Basic Experiment," Mon. Weather Rev., **91**(3), pp. 99–164.

[21] Germano, M., Piomelli, U., Moin, P., and Cabot, W. H., 1991, "A Dynamic Subgrid-Scale Eddy Viscosity Model," Phys. Fluids A Fluid Dyn., **3**(7), pp. 1760–1765.

[22] Lilly, D. K., 1992, "A Proposed Modification of the Germano Subgrid-Scale Closure Method," Phys. Fluids A Fluid Dyn., **4**(3), pp. 633–635.

[23] Boivin, P., 2011, "Reduced-Kinetic Mechanisms for Hydrogen and Syngas Combustion Including Autoignition," Ph.D. thesis, Departamento De Ingeniería Térmica y De Fluidos Escuela Politécnica Superior, Universidad Carlos III de Madrid, Madrid, Spain.

[24] Mechanical and Aerospace Engineering (Combustion Research), University of California at San Diego, 2012, "Chemical-Kinetic Mechanisms for Combustion Applications," San Diego Mechanism, accessed Aug. 22, 2024, https://web.eng.ucsd.edu/mae/groups/combustion/mechanism.html

[25] Goodwin, D. G., Moffat, H. K., Schoegl, I., Speth, R. L., and Weber, B. W., 2022, "Cantera: An Object-Oriented Software Toolkit for Chemical Kinetics, Thermodynamics, and Transport Processes," Version 2.6.0.

[26] Durand, L., and Polifke, W., 2007, "Implementation of the Thickened Flame Model for Large Eddy Simulation of Turbulent Premixed Combustion in a Commercial Solver," ASME Paper No. GT2007-28188.